

This is the accepted manuscript made available via CHORUS, the article has been published as:

Evidence for an internal-field-induced spin-flop configuration in the extended kagome YBaCo_4O_7

M. J. R. Hoch, P. L. Kuhns, S. Yuan, T. Besara, J. B. Whalen, T. Siegrist, A. P. Reyes, J. S. Brooks, H. Zheng, and J. F. Mitchell

Phys. Rev. B **87**, 064419 — Published 22 February 2013

DOI: [10.1103/PhysRevB.87.064419](https://doi.org/10.1103/PhysRevB.87.064419)

Evidence for an internal field induced spin-flop configuration in the extended kagomé YBaCo₄O₇

M.J.R. Hoch¹, P.L. Kuhns¹, S. Yuan¹, T. Besara¹, J.B. Whalen¹, T. Siegrist^{1,2},
A.P. Reyes¹, J.S. Brooks¹, H. Zheng³ and J.F. Mitchell³

¹*National High Magnetic Field Laboratory, Florida State University, Tallahassee, Florida 32310 USA*

²*Department of Chemical and Biochemical Engineering, FAMU/FSU College of Engineering, Tallahassee, Florida 32310 USA*

³*Materials Science Division, Argonne National Laboratory, Argonne, Illinois 60439 USA*

The spin structure and spin dynamics in the extended kagomé frustrated antiferromagnet YBaCo₄O₇, have been investigated using zero field and low applied field ⁵⁹Co NMR. The YBaCo₄O₇ lattice is made up of bipyramid Co-ion units that form alternating planes of edge-sharing spin triangles and corner-sharing kagomé spin triangles in an unusual exchange topology. Our low temperature spin configuration results, based on hyperfine field orientations, are consistent with those from neutron scattering for the triangle spins which order antiferromagnetically below 106 K. For the kagomé spins at low temperatures the static hyperfine fields are found to be oriented orthogonal to those of the triangle spins in a spin-flop configuration that is in disagreement with the neutron findings. Nuclear relaxation rate measurements made as a function of temperature show that inhomogeneous dynamic spin disorder occurs in kagomé planes well below the Néel point.

PACS numbers 75.25.-j, 75.50.Lk, 76.60.Jx

I. INTRODUCTION

Magnetic frustration effects, which involve competing antiferromagnetic (AFM) interactions, can result in interesting spin configurations and unusual physical properties.^{1,2} Examples of geometrical frustration include tetrahedral cluster pyrochlores and corner-sharing spin triangles in kagomé layers.^{3,4} Kagomé systems, with large ground state degeneracy, may form spin liquids at very low temperatures. A recently discovered class of frustrated spin systems is represented by mixed valence $RBaCo_4O_7$ where R is a lanthanide or yttrium ion.⁵⁻⁷ These frustrated systems contain kagomé (K) layers and interdigitated triangular (T) layers giving rise to an exchange topology with both strong interplanar and intraplanar interactions.

In the prototype system, $YBaCo_4O_7$, a structural phase transition, from trigonal (space group $P31c$) to orthorhombic (space group $Pbn2_1$), takes place at 310 K.^{8,9} Below 100 K a small monoclinic distortion occurs linked to strong magnetoelastic coupling.^{8,9} The change in crystal symmetry from trigonal to orthorhombic lifts the geometrical frustration allowing magnetic order to be established at low temperatures. Neutron diffraction has detected long range AFM spin order in $YBaCo_4O_7$ below the accepted value for the Néel temperature $T_N \sim 106$ K.^{8,9} The extrapolated inverse magnetic susceptibility for $T \gg T_N$ gives a Curie-Weiss temperature $\theta_{CW} = -508$ K consistent with a moderate magnetic frustration index ~ 5 .⁸ The neutron diffraction results suggest that AFM ordering of spins occurs in the triangular layers in co-existence with frustrated spin ordering in the kagomé layers.^{9,10} The presence of ferroelastic domains in the ordered AFM phase has been detected in the neutron experiments.⁹

In $YBaCo_4O_7$ the ratio of the Co^{2+} to Co^{3+} ions is 3 to 1. Structural studies suggest that the two types of ions are tetrahedrally coordinated by oxygen.^{6,8} X-ray absorption spectroscopy (XAS) results, together with crystal field calculations for T_d symmetry, show that both Co^{2+} and Co^{3+} are in high spin configurations $S = 3/2$ and $S = 2$ respectively.¹¹ The spin-orbit coupling lifts the ground state degeneracy and for Co^{3+} gives rise to a multiplet of low lying states.¹¹ Neutron diffraction experiments on the related materials $YbBaCo_4O_7$ and

TmBaCo₄O₇ show that the trigonal to orthorhombic transition involves oxygen displacements with tilting and distortion of the tetrahedra.^{6,12} Similar tetrahedral tilting is expected in YBaCo₄O₇. Three crystallographically distinct cobalt sites are present in the K layers in the orthorhombic structure. This feature is important in analyzing our ⁵⁹Co NMR results. It is interesting to note that in non-stoichiometric YBaCo₄O_{7.1} no symmetry lowering phase transformation occurs and the structure remains trigonal at low temperatures.

The present zero field (ZF) and low-field NMR experiments on YBaCo₄O₇, which complement neutron scattering, were undertaken to obtain details of the low temperature spin structure and to determine how spin order and spin dynamics evolve with temperature in this system. Our principal findings are that at low temperatures the majority of K spins are oriented in what can be described as a *spin-flop* configuration with respect to T spins and that as the temperature is raised spins in the K layers become dynamically disordered while those in the T layers preserve AFM order.

II. EXPERIMENTAL

Single crystals of YBaCo₄O₇ were grown in a floating zone furnace at Argonne National Laboratory, and oriented using X-ray Laue diffraction. The ⁵⁹Co NMR measurements were made on both single crystal and crushed polycrystalline YBaCo₄O₇ samples. A pulsed spin-echo NMR spectrometer was used to obtain ZF spectra and relaxation rates in ZF, together with field-perturbed spectra in low applied fields, over the temperature range 0.5 K to 40 K. A helium-3 refrigerator was used for measurements below 1.7 K. In ZF NMR signals are obtained only from nuclei that experience *static* hyperfine (HF) fields B_{HF} on the NMR timescale ($> 10 \mu\text{s}$). The angle θ which the radiofrequency (RF) field $B_1 = \mu_0 H_1$ makes with B_{HF} determines the NMR signal amplitude. A ZF sample rotation experiment, which makes use of this NMR feature, can provide information on both the orientation of ordered spins – or more strictly that of B_{HF} – and on the evolution of dynamical spin disorder with temperature. Rotation spectra patterns obtained in low applied fields can also provide information on the spin structure. The principles of these two sample rotation experiments are given in Section III below.

Figure 1 shows a frequency-swept ZF spectrum, plotted as the integrated spin-echo area versus frequency, for the polycrystalline sample at 2.4 K. The widths Δf of the NMR lines are several MHz and measurements involve hole-burning with the RF bandwidth ~ 300 kHz. The spectrometer frequency was incremented in 0.5 MHz steps in recording spectra. The polycrystalline sample gives a response averaged over all HF orientations with respect to \mathbf{H}_I and provides spectral areas that can be reliably compared. The spectral peaks are identified in Fig. 1 with Co^{2+} and Co^{3+} ions, which can occupy both K and T sites, giving two sets of distinct features that allow novel experiments to be carried out. Details of how the assignments are made are given below.

III. ZERO FIELD AND LOW FIELD NMR IN ANTIFERROMAGNETS

A. Hamiltonian

This discussion focuses on ^{59}Co ZF and low applied field NMR in an AFM system. However, the basic ideas are quite general and should be applicable in a variety of magnetic systems and in systems in which electric quadrupolar interactions are important. The Hamiltonian for ^{59}Co ($I=7/2$, $\gamma_I/2\pi = 10.03$ MHz/T) has the form

$$\mathcal{H} = \mathcal{H}_Z + \mathcal{H}_{\text{HF}} + \mathcal{H}_Q + \mathcal{H}_{\text{RF}}. \quad (1)$$

The Zeeman Hamiltonian \mathcal{H}_Z vanishes in ZF. $\mathcal{H}_{\text{HF}} = \mathbf{I} \cdot \mathbf{A} \cdot \mathbf{S}$ is the hyperfine Hamiltonians with \mathbf{A} the hyperfine tensor. The RF perturbing Hamiltonian is $\mathcal{H}_{\text{RF}} = \gamma_I \hbar \mathbf{I} \cdot \mathbf{B}_1 \cos \omega t$ with ω the RF frequency. \mathcal{H}_Q is the quadrupolar Hamiltonian. No evidence of quadrupolar splitting of the spectra is found which implies $\mathcal{H}_Q \ll \mathcal{H}_{\text{HF}}$. For the case of isotropic hyperfine interactions the Hamiltonian takes the simpler form

$\mathcal{H} = \mathcal{H}_{\text{HF}} + \mathcal{H}_{\text{RF}} = \sum_i A_i \mathbf{I} \cdot \mathbf{S}_i + \gamma_I \hbar \mathbf{I} \cdot \mathbf{B}_1 \cos \omega t$ where the summation over i allows for transferred HF from neighbor Co ions. For ^{59}Co in YBaCo_4O_7 the HF for the various crystal sites is likely to have relatively small

anisotropy. Evidence for this, and for the magnitude of transferred HF contributions from neighboring Co ions, is provided by the relaxation rate results described below. The linewidths of the spectral components shown in Fig. 1 are comparatively large ($\Delta f \sim 5$ MHz) and this reflects the distribution of local hyperfine fields produced by neighboring S spins.

AFM systems with large hyperfine fields and well resolved spectral components allow a novel ZF single crystal rotation experiment to be carried out. For clarity the method will be discussed in relation to YBaCo_4O_7 in which the spins, and therefore the HF fields, are, to a good approximation, confined to the ab crystal plane as shown by neutron diffraction.^{8,9} If the RF field $\mathbf{B}_1 = \mu_0 \mathbf{H}_1$, which is aligned parallel to the RF coil axis, is directed in the ab crystal plane and the crystal is rotated in discrete steps inside the coil, with rotation angle θ specifying the direction of \mathbf{B}_1 measured from a chosen crystal direction, a rotation pattern is generated as shown below in Section IVA. The spin-echo signal depends sensitively on θ since in the two-pulse excitation sequence the transverse nuclear magnetization \mathbf{M}_\perp , which induces the echo signal in the RF coil, is proportional to $\mathbf{M} \times \mathbf{B}_1$. Since \mathbf{M} is parallel to \mathbf{B}_{HF} a maximum signal is obtained when \mathbf{B}_1 and \mathbf{B}_{HF} are orthogonal ($\theta = \pi/2$) and zero when \mathbf{B}_1 is parallel to \mathbf{B}_{HF} ($\theta = 0$). Details of the ZF rotation experiment and associated spectral analysis are given in Section IIIB.

B. Zero applied field rotation experiment

The strong dependence of ZF NMR signals on RF field orientation provides definitive information on \mathbf{B}_{HF} directions at ^{59}Co sites. The hyperfine field is, in general, directed close to anti-parallel to the spin vector for transition metal ions such as Co^{3+} so that determination of \mathbf{B}_{HF} provides information on the spin orientation. Elementary considerations predict that the echo signal should vary as $\sin^\alpha \theta$ with $\alpha > 2$ because of the way the factor $\sin \theta$ occurs in the two-pulse process which induces a spin-echo signal in the RF coil. With a distribution of hyperfine fields the situation is complex. We have carried out a density matrix calculation using the Antiope package¹³ in order to determine the response of the nuclear system to the two-pulse spin-echo

sequence for a range of θ values. This simulation of the rotation experiment provides the form that should be used in fitting the RF field rotation pattern for a system with a \mathbf{B}_{HF} distribution and with variation in the effective \mathbf{B}_1 . For \mathbf{B}_{HF} in the ab plane the following functional form for the echo signal $S(\theta)$ is obtained:

$$S(\theta) = \sin^{2.8}[(\alpha(\pi/2)\sin(\theta+\phi+\eta))\sin(\theta+\phi+\eta)], \quad (2)$$

where ϕ is a phase angle, η sets the rotation zero and $\alpha \sim 1$ allows for small departures in the RF pulse length from the $\pi/2$ condition at the NMR center frequency.

C. Rotation experiment in low applied fields

Information on the spin structure can also be obtained from rotation patterns obtained using relatively small applied magnetic fields which produce a Zeeman perturbation $\mathcal{H}_z = \gamma_I \hbar \mathbf{I} \cdot \mathbf{B}_\nu$ where, typically, $\nu = x, y$ or z . In the present experiments on YBaCo₄O₇ we choose ν in the ab (or xy) plane with z perpendicular to \mathbf{B}_{HF} . The Hamiltonian is $\mathcal{H} = \gamma_I \hbar \mathbf{I} \cdot (\mathbf{B}_{HF} + \mathbf{B}_{ab})$. The NMR spectrum is determined by the vector sum of the applied field and the hyperfine field which leads to a $\cos\theta$ dependent *split* of the spectral components, due to the anti-parallel spin alignments in the AFM sublattices, with θ the angle between \mathbf{B}_{HF} and \mathbf{B}_{ab} .

IV. RESULTS AND DISCUSSION

A. Local hyperfine fields from zero field measurements

The spectral lines in Fig. 1 are well fit by Lorentzians with widths of ~ 3.5 MHz for the 90 and 100 MHz components and ~ 9 MHz for the 120 MHz line. In the spectral assignments use is made of the magnetic moment and spin state information from neutron scattering and XAS experiments.^{9,11} The average moments from the neutron data are $2.63 \mu_B$ for the T spins and $1.89 \mu_B$ for the K spins.⁹ The Co³⁺ ions ($S = 2$) have a moment that is larger than that of Co²⁺ ($S = 3/2$). This information suggests that the high-frequency (80 – 130 MHz) spectra are associated with Co³⁺ ions and the low frequency components, < 70 MHz, with Co²⁺. As we shall see in what follows, these site assignments are supported by the temperature dependences of the spectral

amplitudes, the angular variations of the spectral shapes in applied fields and the relaxation rate behavior with temperature.

The difference between the 90 MHz and 120 MHz K spin peaks is attributed to non-equivalent sites in the K layers linked to tilting or distortion of the oxygen tetrahedra and changes in the $\text{Co}^{3+} S = 2$ manifold of states.¹¹ The 120 MHz line, which shows a broad distribution of hyperfine fields and a linewidth 2.5 times larger than that of the 90 MHz line, is likely a doublet with two similar B_{HF} values. A shoulder at 125 MHz supports the doublet suggestion. The presence of three K spectral components is consistent with the presence of three distinct crystallographic kagomé sites in the orthorhombic structure. Further evidence for three distinct sites is provided by the Co^{2+} spectral components below 70 MHz which show two sharp peaks and a broader peak overlapping one of the sharp peaks. The present experiments have focused on the high frequency region ($f > 70$ MHz), associated with the Co^{3+} ions, because of improved sensitivity ($\propto f^2$). Measurements made at 55 and 62 MHz give similar results to those of the high frequency components.

Figure 2 shows the ZF spectra from 70 – 140 MHz, for a single crystal, scaled with T over the range 4.8 – 20 K. The RF field was directed along the c -axis of the crystal. At low T the area ratios for the 90, 100 and 120 MHz lines are similar to those found for the polycrystalline sample. The observation that for \mathbf{B}_1 along c the single crystal spectral areas are very similar to those of the *orientation independent* polycrystalline material provides strong evidence that the local hyperfine fields are oriented close to the ab plane of the crystal i.e perpendicular to \mathbf{B}_1 . This conclusion is arrived at as follows. For the polycrystalline sample the crystallites are randomly oriented and a spherical average shows that the amplitudes of the various components in the spectra are reduced by the same amount. The amplitude

ratios of spectral peaks for the polycrystalline sample in Fig.1 and for the oriented single crystal in Fig.2, with B_1 along c , are very similar. This suggests that the T and K spin orientations with respect to the c -axis are nearly the same and this finding, together with the neutron scattering results for the orientation of the T spins,⁹ implies that the T and K spins lie in the ab plane. We present further evidence that the T and K spins lie in the ab plane later in the paper.

The NMR signal areas for each component should follow $1/T$ Curie law behavior. Scaling with T may be expected to give constant values but this is not the case for the spectra shown in Fig.2. Over the range 7 – 20 K the T -scaled peaks at 90 MHz and 120 MHz decrease in area by a factor 4 while the scaled 100 MHz peak decreases by roughly 2. The ratio R of the sum of the areas of the 90 and 120 MHz components to that of the 100 MHz component increases with decreasing T and reaches a value $R \sim 2$ at 1.7 K. There are three spins in a K layer for each spin in a T layer. If it is assumed that the Co^{3+} and Co^{2+} ions are randomly distributed then we might expect that $R \sim 3$ will be reached for $T < 1$ K. However, spectra obtained at $T = 500$ mK were similar in form to those measured above 1 K and give a ratio $R < 3$. This result suggests two possible explanations. Firstly, a fraction of the kagomé spins, estimated as 25 - 30 % at 2 K, may remain dynamically disordered at low temperatures and therefore remain undetected in our measurements. Secondly, $R < 3$ may result from non-random occupation of the K and T sites by Co^{3+} associated with some charge ordering of the Co ions. If the Co^{3+} ions show a slight preference for the T sites (which implies that the Co^{2+} ions preferentially occupy K sites) this could account for the observed ratio $R < 3$. It has been suggested that departures from a statistical distribution of the Co^{2+} and Co^{3+} ions between the K and T layers may occur in YBaCo_4O_7 due to ion size effects.⁹ However, analysis of neutron scattering results does not provide convincing evidence for significant charge ordering.^{8, 9} While we cannot rule out the non-random ion distribution explanation for $R < 3$ the relaxation results described in Section IVC, specifically for nuclei associated with the 120 MHz spectral component, suggest that spin dynamical effects persist in the K layers at temperatures down to 0.5 K leading to a reduction in signal from nuclei in these layers. It is important to note that the observed decrease in R with increasing T supports the spectral identifications made in Fig. 1. The decrease in the temperature-scaled

amplitudes of the 90 and 120 MHz components with T , as shown in Fig. 2, is attributed to very short transverse nuclear relaxation times ($<10 \mu\text{s}$) in some regions of the kagomé planes, due to S spin dynamics, rendering ^{59}Co spins in these regions unobservable in spin-echo experiments.

Figure 3 shows the areas of the 90, 100 and 120 MHz spectral components in a ZF single crystal rotation experiment of the type introduced in Section IIIB. Measurements were made at 4 K with the RF field \mathbf{B}_I in the ab plane. The crystal was rotated in discrete steps inside the RF coil with the angle θ specifying the direction of \mathbf{B}_I (parallel to the axis of the RF coil) as measured from the crystal $[110]$ direction in the **hexagonal** primitive cell. As shown in Section IIIB the signals depend sensitively on θ with a maximum when \mathbf{B}_I and \mathbf{B}_{HF} are orthogonal and zero for \mathbf{B}_I parallel to \mathbf{B}_{HF} . The strong dependence of ZF NMR signals on RF field orientation provides definitive information on \mathbf{B}_{HF} directions at ^{59}Co sites, and hence on the relative orientations of the S spins in T and K layers. The Fig. 3 data are well fit with the function given in Eq.(2). In order to fit the data, and specifically to account for the observation that the signal minima are nonzero, it is necessary to allow for the presence of domain structures as revealed by neutron scattering.⁹ Allowance is made for six ferroelastic domains as weighted averages of $\varphi = 0$ and $\pm 2\pi/3$, and for two-fold rotation about the a - axis.⁹ The fit shows that a principal domain contributes $\sim 70\%$ of the signal in our crystal. The remaining 30% is made up of the other domains with some small flexibility in proportions. The dominant role of the principal domain is fortuitous and simplifies the analysis. In particular the major periodic features of the rotation pattern are due to the dominant role played by the principal domain.

The angular dependence in Fig. 3 shows that \mathbf{B}_{HF} for the 100 MHz spins in the T layers is *orthogonal* to \mathbf{B}_{HF} for both the 90 and 120 MHz K spins. The phase agreement of the 90 and 120 MHz rotation patterns is further evidence that the 120 MHz spectral components are associated with K spins at non-equivalent sites to those occupied by the 90 MHz spins. The inset in Fig. 3 gives the calculated rotation pattern for the 5K spin configuration from neutron diffraction⁹ with the assumption that the \mathbf{B}_{HF} at ^{59}Co sites are aligned close to anti-parallel to the associated S spin orientation as stated above. Allowance is made for six domains with domain

fractions, for consistency, chosen the same as in the NMR fit. The neutron spin structure predictions are in excellent agreement with the NMR rotation pattern for the T spins but not for the K spins (see inset in Fig.3). The NMR results show that the T spins lie close to or in the ab plane perpendicular to the primitive cell $[110]$ direction while the static K spins lie roughly parallel to $[110]$. The disagreement in K spin orientations determined using neutron diffraction and those from the NMR hyperfine fields is not clear at present.

It is interesting to note that the ^{59}Co ZF NMR spectra for a non-stoichiometric single crystal of $\text{YBaCo}_4\text{O}_{7+\delta}$ ($\delta = 0.1$), containing excess oxygen, show a broad distribution of frequencies (50 to 140 MHz) produced by a distribution of static hyperfine fields, on the NMR time scale, at low temperatures. The spectra exhibit a maximum at around 100 MHz. and show no detectable dependence on orientation in the RF field. The results suggest that the spins are frozen in a spin glass type configuration. Unlike YBaCo_4O_7 this material does not undergo a symmetry lowering transition from trigonal to orthorhombic. Further experiments on $\text{YBaCo}_4\text{O}_{7+\delta}$ are planned.

B. Hyperfine field configurations from low applied field measurements

In-field rotation patterns, derived from field-induced splits of the spectral components for the YBaCo_4O_7 single crystal, have been made to complement the ZF results. The RF field was directed along the c axis with the applied field $\mathbf{B} \ll \mathbf{B}_{\text{HF}}$ in the ab plane. Crystal orientations θ with respect to the applied field were measured from the $[110]$ direction. Figure 4 shows representative spectra as a function of \mathbf{B} for $\theta = 90^\circ$. As can be seen the 100 MHz component, which is associated with the T spins, splits into two as described in Section IIIC for an AFM system in a field directed along the spin alignment direction for one sublattice. Note that the dominant lines are due to the principal domain with subsidiary components arising from the other domains. These features were allowed for in fits to the rotation pattern spectra described below. The split Δf in the 100 MHz component exhibits a linear field dependence depicted in the inset in Fig. 4. The line through the points has the predicted slope $^{59}\gamma_{\text{I}} = 10.03 \text{ MHz / T}$ for ^{59}Co nuclei. For $B < 1.0 \text{ T}$ the 90 MHz and 120 MHz K principal domain components remain unchanged at this crystal orientation which implies that the K hyperfine

fields are orthogonal to \mathbf{B} and therefore to the T hyperfine field. Note that the small split of 12.5 MHz (0.25 T) found for the 90 MHz component at $B = 1.5$ T is due to K spins not being exactly aligned perpendicular to [110] but an angle of roughly 10° from [110]. This offset is clear in the rotation pattern for $B = 0.5$ T that is presented below. Further evidence that the spins lie in, or close to, the ab plane was obtained in a separate experiment in which a field of 1 T was aligned parallel to the c -axis and no detectable split of any of the spectral components was found.

Figure 5 shows spectra for $B = 0.5$ T at $\theta = 0^\circ$, -40° and -90° , which illustrate how the split in the components varies with orientation. The spectra were fit using multiple Lorentzian functions $L_i(f_{0i}, \Delta f_{0i}, B, \theta)$ in an expression of the form $S(f) = \sum_i A_i L_i(f_{0i}, \Delta f_{0i}, B, \theta)$ where the sum over i includes all spectral components, including those associated with domains, with f_{0i} the fixed center frequency for component i , Δf_{0i} the linewidth and A_i an amplitude parameter. Excellent fits to the measured spectra were obtained with domain fractions again 70% for the principal domain and the remaining 30% distributed amongst the other domains. Based on fits to a complete set of 0.5 T rotation spectra, Fig. 6 shows the angular dependence of the peak frequencies for the principal domain components of the ZF 90 MHz and 100 MHz lines. The rotation patterns are well fit with cosine and sine functions respectively, as shown, with details given in the figure caption. It is clear from Fig. 6 that the K and T hyperfine fields are *orthogonal* to one another consistent with the conclusion reached on the basis of the ZF rotation experiments in Section IVA. Again the T hyperfine fields are found to be close to perpendicular to the [110] direction in the hexagonal primitive lattice cell and with the assumption that \mathbf{B}_{HF} is anti-parallel to \mathbf{S} the NMR findings are in good agreement with the neutron diffraction results. The orthogonal configuration of the K and T hyperfine fields suggests that a spin-flop of K spins is induced by the local field due to coupling to nearby AFM ordered T spins. The resultant spin arrangement, based on the NMR analysis, is schematically depicted in Fig. 7(a) while Fig. 7(b) shows the spin configuration for representative adjacent T and K layers obtained from neutron diffraction as given in Ref. (9). The NMR and neutron spin configuration findings are in excellent agreement for the T spins, which exhibit

long range order at low temperatures, but not for the K spins. The disagreement between the neutron and NMR findings for the K spins is unexpected and remains to be explained. Note that in Fig. 7(a) each kagomé triangle has two spins aligned parallel to each other with the third spin aligned antiparallel. In this spin arrangement it is possible that adjacent bipyramid units in small clusters have their spins arranged to give zero net spin $\sum_i S_i = 0$ in a configuration that minimizes the cluster magnetic energy. The five Co ion spins in a trigonal bipyramid are not mutually connected and this permits the $\sum_i S_i = 0$ rule^{1, 10} to not apply to a single bipyramid.

C. Relaxation rates and spin dynamics

The spin-lattice relaxation time T_1 and the spin-spin relaxation time T_2 were measured as a function of T and the corresponding relaxation rates at 90, 100 and 120 MHz are shown in Figs. 8(a) and 8(b). Similar relaxation rate results are obtained for the low f spectra. The data in Figs 8(a) and in 8(b) show similar trends for the three frequencies. However, in the range $4 < T < 12$ K the 90 and 120 MHz (K-spin) rates are significantly higher than the 100 MHz (T-spin) values, by factors 3 and 10 respectively. The high values of the relaxation rates for the K components are consistent with dynamical spin reorientation occurring in the K planes. The similarity in behavior of $1/T_1$ and $1/T_2$ with T , as shown in Figs. 8 (a) and (b), points to common underlying relaxation mechanisms and an important role for fluctuating transferred hyperfine field contributions, from neighbor ions, which determine $1/T_1$ and $1/T_2$. Note that for $T < 4$ K the longitudinal and transverse relaxation rates of each component differ by more than an order of magnitude. This implies that the fluctuating longitudinal hyperfine field B_{HF}^{\parallel} is larger than the fluctuating perpendicular component B_{HF}^{\perp} consistent with some hyperfine anisotropy as given below.

From Fig. 8(b) we see that there are three regions in which the relaxation rates exhibit markedly different T dependences. In region I ($T < 4$ K) the behavior follows $1/T_1 = AT^{\nu}$, with $\nu \sim 3$ as shown by the straight lines of slope 3 in the log plot, consistent with a process involving magnon scattering.^{16, 17} The similar low- T

relaxation behavior found at 90 MHz and 100 MHz, for K and T ^{59}Co nuclei respectively, implies dynamical coupling between the layers through transferred hyperfine fields. The $1/T_1$ behavior of the 120 MHz components at temperatures below 4 K is clearly different to that of the other components. Figure 8(b) shows that the temperature range over which spin waves dominate in relaxation is rather limited. For AFM systems in which spin waves determine $1/T_1$ the following expression applies for Raman two-magnon processes in 3D systems.^{16,17}

$$\frac{1}{T_1} = \frac{CA^2}{(2\pi)^3 \hbar^2 \omega_e} \left(\frac{k_B T}{\hbar \omega_e} \right)^3 I(x). \quad (3)$$

C is a constant of order unity and $\hbar \omega_e = 2zJS$ where J is the exchange coupling between spins S and z is the number of nearest neighbors. The definite integral $I(x)$, with $x = (E/k_B T)$ and E the spin wave energy, has a maximum value $\pi^2/6$ in the high T limit and at lower T can be expressed in terms of the Debye integral.¹⁷ The cross-over temperature from high to intermediate is given by $k_B T_{AE} = 2S\sqrt{zJK}$ with K the anisotropy constant. Using rough estimates for $2zJS = T_N$ and $K \sim 0.1$ K we obtain an upper limit for $T_{AE} \sim 2$ K. We estimate $\omega_e \sim 10^{13} \text{ s}^{-1}$, based on the observed T_N value, while from the observed resonance frequency $\omega_{HF} = A/\hbar \sim 6 \times 10^8 \text{ s}^{-1}$. Inserting these values in Eq. (3) gives $1/T_1 \sim 20 \text{ ms}$ at 4 K in fair agreement with the observed value for the 100 MHz T component. The ^{59}Co relaxation behavior is consistent with the spin wave mechanism being dominant, for $T \leq 4$ K, at both 100 MHz and 90 MHz. As mentioned above the 120 MHz relaxation rate T -dependence is clearly different to that of the two lower frequency components pointing to a mechanism other than spin waves playing the key role at 120 MHz. A simple model for this behavior is discussed below. The $1/T_2$ behavior with T is similar to that of $1/T_1$ for each of the three components but with the values higher by roughly an order of magnitude consistent with theoretical predictions for relatively small anisotropy ($\sim 10\%$) in the hyperfine field.¹⁶

In region II, ($4 < T < 10$ K) of Fig. 8(b), the magnon scattering processes lose their effectiveness and the rates increase gradually with distinctly different behavior to that of region I. In region III, $T > 10$ K for the K spins, and $T > 15$ K for the T spins, the rates increase more rapidly with rising T pointing to significant changes in the spin-spin correlation function.¹⁸

The magnetization M of our single crystal sample is shown versus T in a semilog plot in Fig. 9. Measurements were made using a SQUID magnetometer in a field of 0.1 T applied firstly in the ab plane 15° from $[110]$ and secondly along the c -axis. The temperatures indicated by arrows correspond, respectively, to the onset of long range ordering at T_N and to a spin reorientation transition at T_R .⁹ Note that M_{ab} decreases gradually with T from 2 – 10 K, passes through a minimum and then increases from 12 – 50 K. M_c follows a similar trend to M_{ab} below 10 K exhibits a plateau in the range 10 – 35 K and decreases at higher temperatures. The straight line drawn through the lowest temperature points for M_{ab} shows that a gradual change in magnetization behavior with rising T occurs above 4 K. This behavior is consistent with the onset of some dynamical spin disorder for $T > 4$ K. The present relaxation rate results suggest that dynamical disorder is linked to the K spins.

Over a wide range of temperature T_1 recovery curves have stretched exponential form $\exp[-(t/T_1)^\beta]$, with $\beta \sim 0.5$, due to a distribution of relaxation rates in this inhomogeneous system.¹⁹ Some variation in spin dynamics across K planes is likely. The T_2 spin-echo decay curves also show stretched exponential form with a somewhat higher value for $\beta \sim 0.7$. It is instructive to note that the spin-echo amplitudes at $t = 0$, obtained from the fitted echo amplitude versus pulse spacing curves at each temperature, decrease in an unusual way with T as shown in the inset in Fig. 8(a). The solid curve gives Curie law behavior. Significant departures from Curie law behavior that occur above 4 K are linked to lineshape changes which result in an increase in the echo amplitude. Line narrowing with rising T above 4 K has been found from fits made to the 90, 100 and 120 MHz spectral lines with fractional changes in Δf of 35 %, 30% and 70 % respectively over the range 4 – 20 K. The changes in linewidth imply changes in the transferred hyperfine field distribution due to changes in the spin dynamics. These changes in dynamics determine the behavior with temperature of the relaxation rates. (Note

that the area under a spectral line is a more reliable measure of the number of spins observed than is the signal amplitude. This point is important in considering the spectra shown in Fig.2.) Irreversible behavior of $1/T_1$ is found above 15 K and the data shown were obtained in warming runs.

Following on the above discussion it is likely that in regions II and III, as shown in Fig. 8, spin dynamics with a distribution of spin correlation times provides the relaxation mechanism for Co nuclei through dynamical intersite hyperfine coupling. If the S spin correlation function for spins j in a given region of the crystal has exponential time dependence the relaxation rate is given by¹⁸

$$\frac{1}{T_{1i}} = \gamma_i^2 \sum_j B_j^2 \left(\frac{\tau_j}{1 + \omega_0^2 \tau_j^2} \right) \approx \gamma_i^2 \bar{B}^2 \left(\frac{\bar{\tau}}{1 + \omega_0^2 \bar{\tau}^2} \right) \quad (4)$$

$\bar{B}^2 = \bar{A}^2 / \gamma_i^2 \hbar^2$ is the average transverse fluctuating effective field at site i due to n neighbor spins j with average correlation time $\bar{\tau}$. (Distribution functions for correlation times and fluctuating local fields could be considered and summed over but this procedure introduces additional parameters and does not provide additional insight.) Note that Eq. (4) predicts a maximum in $1/T_1$ for $\omega_0 \bar{\tau} = 1$ while in the short correlation time limit $1/T_1 = \gamma_i^2 \bar{B}^2 \bar{\tau}$ where, to simplify the notation, the subscript i has been dropped. An expression for $1/T_2$, similar in form to Eq. (4), contains contributions from both transverse and low frequency longitudinal local field fluctuations.¹⁹ The present discussion will focus on the $1/T_1$ results.

At $T \sim 15$ K, for which $1/T_1 \sim 10 \text{ ms}^{-1}$ for the 90 MHz component, we estimate the correlation time to be $\bar{\tau} \sim 10^{-5} - 10^{-6}$ s. This value gives $\bar{B} \sim 0.1$ T for the fluctuating local field that produces nuclear relaxation in the kagomé planes. Taking the moment of a K spin as $\mu = 1.89 \mu_B$ gives the single ion dipolar field $\mu/r^3 \sim 0.35$ T for $r = 0.4$ nm which is of the order of a lattice spacing. It is likely that a number of S spins at various distances of the order of a few lattice spacings from site i contribute to relaxation. The numerical estimates are consistent with fluctuating S spin dipolar hyperfine fields providing the relaxation mechanism in temperature

ranges II and III. The plots in Fig. 8(b) show that the relaxation rates continue to increase with rising T . This implies that $\omega_0 \bar{\tau} > 1$ for the temperature range involved. The distribution of correlation times, which follows from the stretched exponential form of the nuclear magnetization recovery curves, allows that some spins or correlated clusters have τ values significantly shorter than the mean value.

The K spins, particularly those associated with the 120 MHz spectral component, play a key role in determining the spin dynamics in the system. The $1/T_1$ values are highest for this component and the spectral area decreases more rapidly with rising T than that of the 90 and 100 MHz spectral lines. The 120 MHz K spins provide relaxation sinks to the lattice and may promote disorder in adjacent regions of the kagomé planes as T is raised.

The evidence from the behavior of spectral areas and relaxation rates with increasing T suggests the following dynamical model for YBaCo_4O_7 . At the lowest temperatures below 1 K relatively long correlation time spin fluctuations occur in correlated spin cluster regions of varying size involving primarily, but not exclusively, the 120 MHz K spins. With increasing temperature $\bar{\tau}$ for these clusters decreases and the dynamically disordered regions increase in size and/or number. Above 4 K the 2D dynamical disorder sufficiently affects the 90 MHz K spins leading to disruption of the spin wave relaxation mechanism in this temperature range. From 4 – 20 K the relaxation rates for the 100 MHz T and 90 MHz K spectral components track that of the 120 MHz K component whose fluctuating spins appear to drive the relaxation process. For $T > 12$ K the relaxation rates increase significantly resulting in a decrease in the signal /noise ratio for the 120 MHz component. Above 15 K it is likely that spin clusters become less correlated and the kagomé planes tend towards a 2D viscous spin liquid phase.

The model accounts for the NMR results as follows. For $T < 4$ K the electron spins in the T planes are AFM ordered and significant areas of the K planes are correspondingly aligned in a spin-flop configuration. Spin

waves in the T and /or K layers are detected through the nuclear relaxation rate measurements. Above 4 K, 2D regions of dynamical disorder in K planes become important. The disorder arises as a result of thermal excitation of low energy modes such as weather vane modes in hexagon loops and other spin cluster dynamics that can occur in kagomé AFM systems.^{20,21} Regions with short S spin correlation times τ , on the NMR time scale, have short ^{59}Co T_2 values which reduce spin-echo amplitudes and lead to the decrease in area of K lines. With rising T the τ distribution in disordered regions shifts towards shorter times. ^{59}Co nuclei in highly dynamical regions no longer contribute to NMR spectra and the correlation time distribution, for the spins in regions that contribute to the signals, is effectively truncated at a limiting value $\tau_{\min} \sim 10^{-5} - 10^{-6}$ s for ZF ^{59}Co observation. In addition to the loss of spectral amplitude, truncation of the broad τ distribution is consistent with the plateau in ^{59}Co rates in region II of Fig. 4. The behavior of the 100 MHz T spectra and relaxation rates with T reflects that of the K layers. S spin fluctuations in regions of the K layers couple via dipolar interactions to nearby ^{59}Co in the T layers. Neutron scattering detects long range AFM order for T approaching 100 K which shows that the T layers do not undergo 2D melting in the same way as suggested above for the K layers. Rather, the fluctuating fields due to the short τ K spins in disordered regions, or viscous spin liquid puddles, reduce T_2 for nuclei in neighbor T layers resulting in a diminution of their spin-echo signals.

It is of interest to note that the spin dynamics behavior found in the present work on YBaCo_4O_7 is in complete contrast to Mössbauer spectroscopy and neutron scattering results on the related extended kagomé system $\text{YBaCo}_3\text{FeO}_7$. On the Mössbauer timescale the Fe^{3+} ions in the triangular layers in $\text{YBaCo}_3\text{FeO}_7$ order below 50 K while the Fe^{3+} in kagomé layers remain ordered at much higher temperatures.²² For YBaCo_4O_7 the changes in the NMR spectra and in the relaxation rates with temperature in the range 4 - 20 K provide compelling evidence for spin dynamics in a fraction of sites in the K layers. Dynamic disorder increases with rising temperature but the NMR signals that are observed are due to those regions that are static on the NMR time scale. It appears that the K layers behave in an inhomogeneous way and further work is needed in order to gain a deeper understanding

of the underlying physics. One possibility is local oxygen non-stoichiometry which enhances local spin dynamics. Some supporting evidence for this possible mechanism has recently been obtained in experiments on a non-stoichiometric crystal.

V CONCLUSION

Our experiments show that ^{59}Co NMR in ZF can distinguish Co-ions in different valence states and between kagomé and triangular layer sites. Furthermore, spectral features from non-equivalent kagomé sites in the monoclinically distorted orthorhombic lattice can be distinguished. Nuclear relaxation rates allow the Co ion spin dynamics to be probed as a function of temperature. These results, together with changes in spectral areas with T , show that on the NMR time-scale 2D progressive ‘melting’ of K layers occurs for $T > 4$ K while the T layers remain AFM ordered. A model for the spin dynamical processes is proposed. Information on the low temperature ($T < 4$ K) hyperfine field orientations at different sites, which are closely related to spin directions at these sites, is obtained from unconventional single crystal hyperfine field rotation experiments in zero applied field. The findings are supported by single crystal rotation measurements in an applied magnetic field of 0.5 T. An important result at low T is that the static hyperfine fields in the T and K layers are close to *orthogonally* oriented with respect to each other consistent with an internal field induced spin -flop process for the frustrated K spins.

ACKNOWLEDGMENTS

Discussions with W.G. Moulton are gratefully acknowledged. The work was supported by the NSF under Cooperative Agreement DMR-0654118 and by the State of Florida. JSB acknowledges funding from NSF-DMR 1005293. Work at Argonne was supported by the US DOE, Office of Science, under contract DE-AC02-06CH211357.

- ¹ R. Moessner, and A.P. Ramirez, Phys. Today **59**, 24 (2006).
- ² J.S. Gardner, M.J.P. Gingras, and J.E. Greedan, Rev. Mod. Phys. **82**, 53 (2010).
- ³ R. Moessner, and J.T. Chalker, Phys. Rev. B **58**, 12049 (1998).
- ⁴ O. Tchernyshyov, R. Moessner, and S.L. Sondhi, Phys. Rev. Lett. **88**, 067203 (2002).
- ⁵ M. Valldor, and M. Andersson, Solid State Sci. **4**, 923 (2002).
- ⁶ A. Huq, J.F. Mitchell, H. Zheng, L.C. Chapon, P.G. Radaelli, K.S. Knight, and P.W. Stephens, J. Solid State Chem. **179**, 1136 (2006).
- ⁷ D.D. Khalyavin, P. Manuel, J.F. Mitchell, and L.C. Chapon, Phys. Rev. B **82**, 094401 (2010).
- ⁸ L.C. Chapon, P.G. Radaelli, H. Zheng, and J.F. Mitchell, Phys. Rev. B **74**, 172401 (2006).
- ⁹ D.D. Khalyavin, P. Manuel, B. Ouladdiaf, A. Huq, P.W. Stephens, H. Zheng, J.F. Mitchell, and L.C. Chapon, Phys. Rev. B **83**, 094412 (2011); D.D. Khalyavin et al., Phys. Rev. B **83**, 219902(E) (2011).
- ¹⁰ P. Manuel, L.C. Chapon, R. Radaelli, H. Zheng and J.F. Mitchell, Phys. Rev. Lett. **103**, 037202 (2009).
- ¹¹ N. Hollmann, Z. Hu, M. Valldor, A. Maignan, A. Tanaka, H.H. Hsieh, H.-J. Lin, C.T. Chen, and L.H. Tjeng, Phys. Rev. B **80**, 085111 (2009).
- ¹² D.D. Khalyavin, L.C. Chapon, P.G. Radaelli, H. Zheng, and J.F. Mitchell, Phys. Rev. B **80**, 144107 (2009).
- ¹³ F.S. de Bouregas and J.S. Waugh, J. Mag. Res. **96**, 280 (1992). (The density matrix package used in the present calculations is ANTIOPE version 3.2.)
- ¹⁴ T. Moriya, J. Phys. Soc. Japan **18**, 516 (1963).
- ¹⁵ T. Imai, C.P. Slichter, K. Yoshimura and K. Kosuge, Phys. Rev. Lett. **70**, 1002 (1993).
- ¹⁶ T. Moriya, Prog. Theor. Phys. **16**, 23 (1956); T. Moriya, Prog. Theor. Phys. **16**, 641 (1956).
- ¹⁷ D. Beeman, and P. Pincus, Phys. Rev. **166**, 359 (1968).
- ¹⁸ C.P. Slichter, *Principles of Magnetic Resonance* 3 rd ed. Ch. 5 (Springer-Verlag, Heidelberg, 1996).
- ¹⁹ D.C. Johnston, Phys. Rev. B **74**, 184430 (2006).
- ²⁰ J.N. Reimers and A.J. Berlinsky, Phys. Rev. B **48**, 9539 (1993).
- ²¹ W. Schweika, M. Valldor and P. Lemmens, Phys. Rev. Lett. **98**, 067201 (2007).
- ²² M. Valldor, R.P. Hermann, J. Wuttke, M. Zamponi and W. Schweika, Phys. Rev. B **84**, 224426 (2011).

Figure captions

FIG. 1 (color online) ^{59}Co zero field NMR spectrum for a YBaCo_4O_7 polycrystalline sample at 2.4 K. The spectral peaks are identified by the valence states of the Co ions in kagomé and triangular plane lattice sites. The inset shows the Co-ion lattice. The shaded areas depict the kagomé planes.

FIG. 2 (color online) ^{59}Co zero field NMR spectra obtained for a single crystal of YBaCo_4O_7 over the temperature range 4.8 to 20 K. The RF field is directed along the crystal c -axis. Spectral amplitudes have been scaled by T to compensate for the Boltzmann factor. The observed decrease in scaled amplitudes with T is attributed to spin dynamics in kagomé planes.

FIG. 3 (color online) ZF ^{59}Co NMR spectral areas for a YBaCo_4O_7 single crystal vs. angle θ between the RF field direction in the ab plane and the crystal $[110]$ axis. The full fitted curves are based on a model described in the text. The observed phase shift shows that kagomé plane ^{59}Co hyperfine fields (90 and 120 MHz) are orthogonal to those of the triangular plane (100 MHz). The inset shows model predictions based on the spin configuration from neutron diffraction. [9] While the NMR and neutron results agree for the triangle layers there are clear differences for the kagomé layers.

FIG. 4 (color online) ^{59}Co NMR spectra for a single crystal of YBaCo_4O_7 as a function of applied field $\mu_0\mathbf{H}$, in the range 0 – 1.5 T, directed parallel to $[110]$ in the ab plane. The RF field \mathbf{B}_1 is directed along the c -axis. The major peaks at 90, 100 and 120 MHz in ZF are associated with the dominant (70 %) domain. The applied field induces a split Δf in the ZF 100 MHz component but not in the principal domain 90 or 120 MHz components. The split in the subsidiary peaks shown is due to the 30 % of smaller domains as discussed in the text. Predicted unbroadened line spectra for the 1.5 T case are shown in the box region at the top of the figure. For the chosen orientation the frequencies of the various components are calculated as described in Section IIIB. The inset in

Fig. 4 gives a plot of Δf versus $\mu_0 H$ which shows a linear relationship. The line drawn through the points has slope 10.03 MHz / T, the γ_I value for ^{59}Co .

FIG. 5 (color online) ^{59}Co NMR spectra for a YBaCo_4O_7 single crystal in an applied field $\mu_0 H = 0.5$ T directed at three different orientations, $\theta = 0^\circ$, 50° and 90° , with respect to $[110]$. For $\theta = 90^\circ$ the K spin component (at 90 MHz in ZF) is split while for $\theta = 0^\circ$ the T spin component (at 100 MHz in ZF) is split. This behavior shows that the T and K hyperfine fields are orthogonal to one another. At the intermediate orientation of 50° both spectral components split.

FIG. 6 (color online) Angular dependence of the ^{59}Co NMR spectral peak frequencies f , for the two principal components, 90 MHz K spins and 100 MHz T spins, for an YBaCo_4O_7 single crystal in ZF. The angle θ , is measured from $[110]$ in an applied field $\mu_0 H = 0.5$ T in the ab plane. The spectral peak frequencies were obtained from Lorentzian multipeak fits to the spectra as described in the text. The upper two curves have the form $f = 99.6 + 5 \cos(\theta + \phi)$ with phase shifts $\phi = 0$ and π , while the lower curves are given by $f = 89 + 5 \sin(\theta + \phi)$ with phase shifts 0 and π . The rotation pattern shows that the K spin and T spin hyperfine fields are orthogonal to one another.

FIG. 7 (color online) **(a)** Spin configuration for the T and K spins in YBaCo_4O_7 at 4 K as derived from the NMR hyperfine field measurements. Co ions in the T layers are represented in blue and those in the K layers in red while the inset in Fig. 7(a) shows the $[110]$ crystal direction for a hexagonal primitive cell. It is suggested in the text that the K layer spin-flop configuration is induced by coupling to the AFM ordered T layer spins. **(b)** Spin configuration based on neutron diffraction results for a single crystal of YBaCo_4O_7 at 5 K as given in Ref. (9).

FIG. 8 (color online) (a) ^{59}Co spin-spin $1/T_2$ and (b) spin-lattice $1/T_1$ relaxation rates for polycrystalline YBaCo_4O_7 as a function of T , at 90, 100 and 120 MHz. Regions shown as I, II and III exhibit markedly different behavior. Spin wave scattering dominates in relaxation in region I below 4 K. The straight lines shown in region I of Fig. 8(b) each has the form $1/T_1 \propto T^3$ as predicted by theory (Ref. 17) for AFM systems. At higher T , in regions II and III, the rates reflect 2D dynamical spin disorder in kagomé planes. The inset in Fig. 8(a) shows $t = 0$ spin echo amplitudes as a function of T . The full curve is Curie's law which gives a fit to the data below 4 K. The relaxation rate plateau from 4 – 12 K is accompanied by changes in spectral linewidth as discussed in the text.

FIG. 9 (color online) Magnetization M versus T plot for the single crystal YBaCo_4O_7 sample. Measurements were made using a SQUID magnetometer with the applied field firstly in the ab plane close to the $[110]$ direction and secondly parallel to the c -axis. The temperature T_N marks the onset of long range magnetic order as determined by neutron scattering while T_R corresponds to a spin reordering transition. The dashed lines at 4 K and 12 K indicate temperatures at which changes in the relaxation rates occur for increasing T as shown in Fig.8. The straight line drawn through the low T points for the ab plane data shows the onset at 4 K of a change in the ab plane magnetization behavior, from an initial gradual decrease with T to an increasing trend which continues above 12 K.

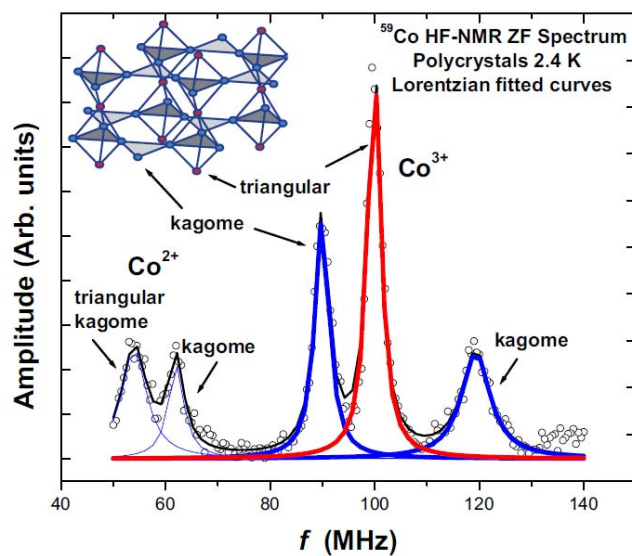


Figure 1

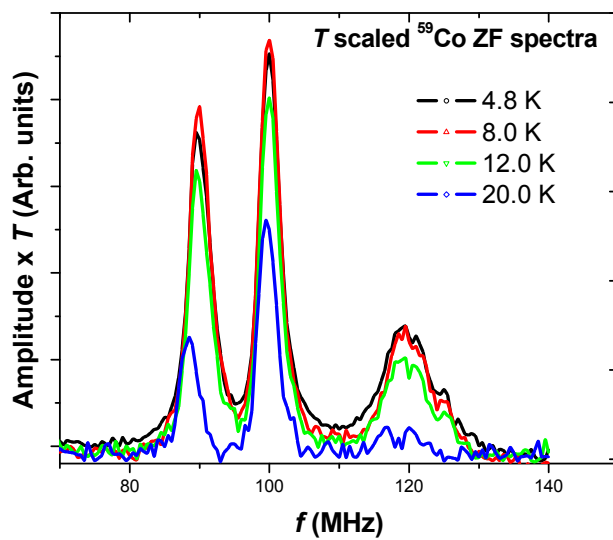


Figure 2

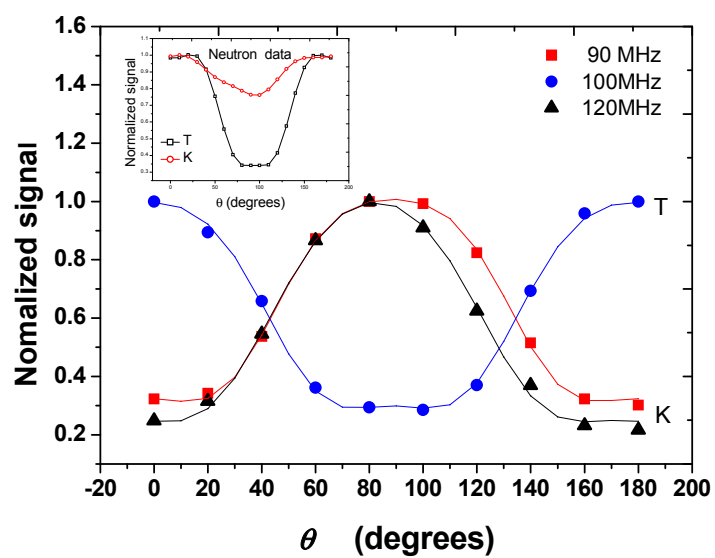


Figure 3

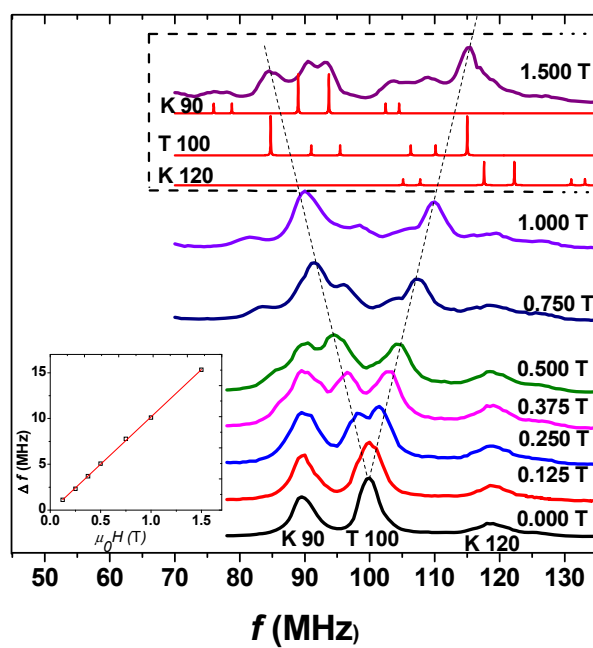


Figure 4

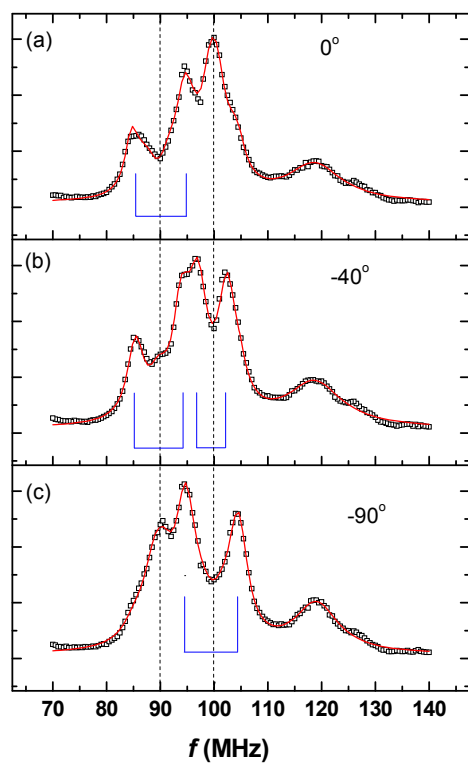


Figure 5

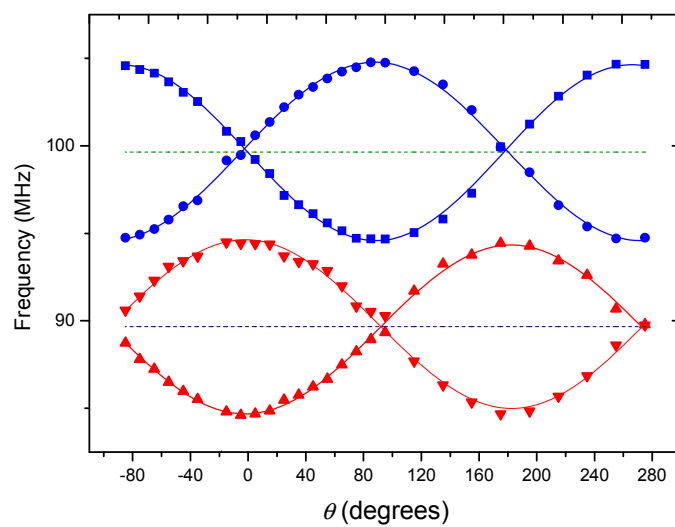


Figure 6

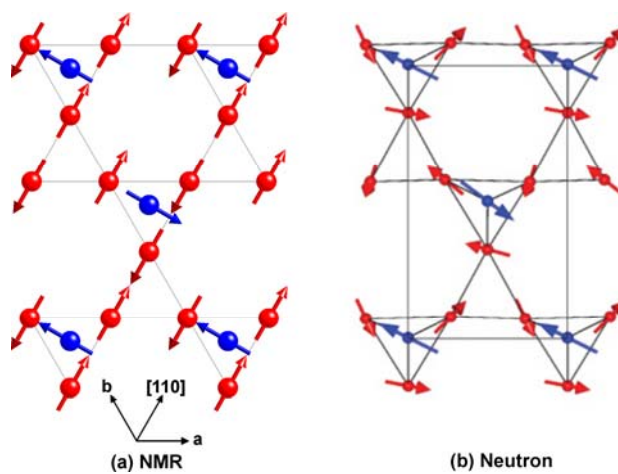


Figure 7

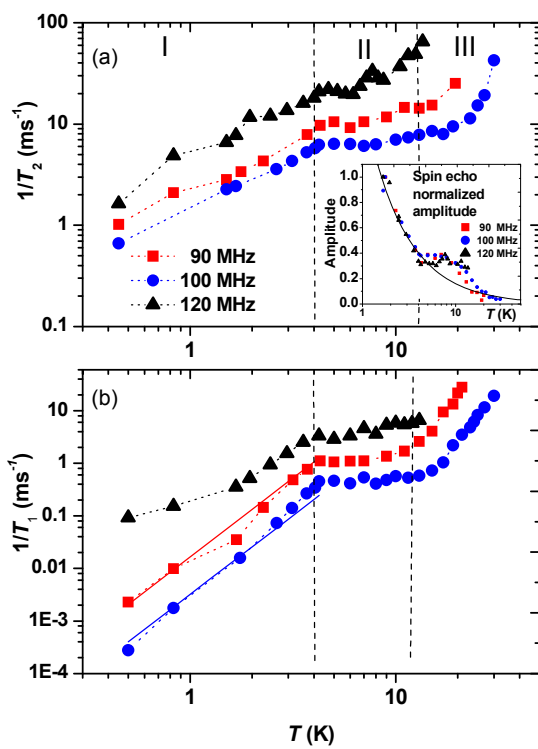


Figure 8

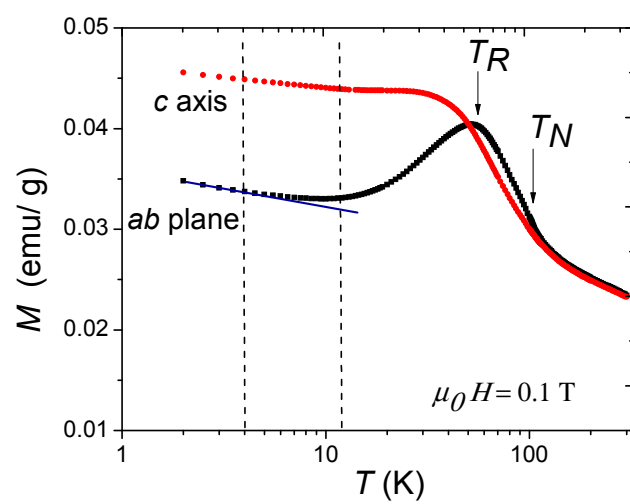


Figure 9